THE JOURNAL OF
PHYSICAL CHEMISTRY C

Article

pubs.acs.org/JPCC

Hydrogen Physisorption on Carbon Foams upon Inclusion of Many-Body and Quantum Delocalization Effects

A. Martínez-Mesa,[†] L. Zhechkov,[‡] S. N. Yurchenko,[§] T. Heine,[‡] G. Seifert,*[,∥] and J. Rubayo-Soneira[⊥]

[†]Departmento de Física Teórica, Universidad de la Habana, San Lázaro y L, La Habana 10400, Cuba
[‡]Jacobs Unversity, School of Engineering and Science, D-28725 Bremen, Germany
[§]University College London, London, United Kingdom
[∥]Technische Universität Dresden, Institut für Physikalische Chemie, D-01062 Dresden, Germany
[⊥]Instituto Superior de Tecnologías y Ciencias Aplicadas, Ave. Salvador Allende y Luaces, Quinta de Los Molinos, La Habana 10600, Cuba

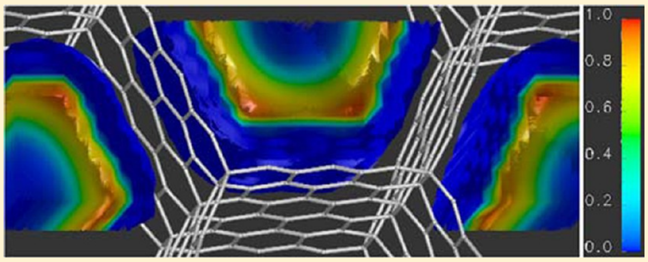

ABSTRACT: We investigate the effect of the structural characteristics of idealized nanoporous environments on the adsorption of molecular hydrogen. The storage capacities of the (n,n) armchair and zigzag carbon foams (n = 2−5) are evaluated in a broad range of thermodynamic conditions. Our calculations are performed within an extension of the density functional theory of liquids to quantum fluids at finite temperature (QLDFT) of particles obeying Bose−Einstein statistics. The exchange-correlation (excess) functional is derived from the empirical equation of state of the homogeneous system. Graphitic foams are found to exhibit hydrogen uptakes similar to other carbonaceous materials, the largest gravimetric capacity being that of the (5,5) zigzag structure (~4.5% at T = 77 K). The storage properties show a rather smooth dependence on the size of the pore. The effects of the H_2−H_2 interactions on adsorption isotherms are evaluated via the comparison of QLDFT results with calculations based on the ideal gas approximation.

I. INTRODUCTION

During the last few decades, many experimental and theoretical investigations[1−10] have been devoted to understanding the process of light molecule adsorption in nanoporous materials. The interest in the evaluation of molecular diffusion rates and storage capacities has been enhanced by several related technological applications like molecular sieving,[11,12] reduction of carbon dioxide emissions by vehicles,[13] or fuel cells.[9] In spite of being a renewable and environmentally friendly energy source, mobile applications using molecular hydrogen as fuel are presently limited by the lack of efficient lightweight hydrogen storage devices. As a consequence, technological limits have been established for the design of efficient storage media. These limits concern both the adsorbed molecular density n_{ads} and the gravimetric capacity gw, i.e., the ratio between the weight of adsorbed hydrogen and the total weight of the system. They are recommended by the US Department of Energy (US DoE) to exceed 40 kg/m^3 and 5.5%,[14] respectively. Carbon containing frameworks are among the usual targets of the above investigations, owing to their low molecular weight and great stability. Albeit presenting hydrogen binding abilities lower than more complex nanostructured substances such as metal−organic and covalent−organic frameworks, pure carbonaceous materials remain as widespread models for the study of the adsorption in porous media.

Contrary to chemisorption, in the process of molecular physisorption, the guest molecules interact only weakly with the surface of the host material by means of London dispersion forces. Due to the reversibility and fast kinetics of the physisorption process, it offers a promising alternative for developing novel hydrogen storage technologies for transport applications. Although the hydrogen storage capacity of carbon nanostructures in the physisorption regime has been measured by several groups, the experimental results show broad variations caused by a variety of factors, as for example the strong dependence on the pretreatment of the samples.[15−19] Such deviations, together with the ambiguity in the interpretation of the data, introduced by the heterogeneities of the internal surface and the relatively wide distribution of pore sizes present in realistic porous materials, stress the importance of theoretical investigations in general and computer simulations particularly to understand the microscopic mechanism underlying storage properties. On the other hand, to constitute reliable models of the H_2 uptake, theoretical approaches must incorporate the quantum nature of these light molecules.[20] Since deviations from Boltzmann statistics are negligible at temperatures of interest for practical applica-

Received: June 4, 2012
Revised: August 17, 2012
Published: August 20, 2012

dx.doi.org/10.1021/jp305462w | J. Phys. Chem. C 2012, 116, 19543−19553

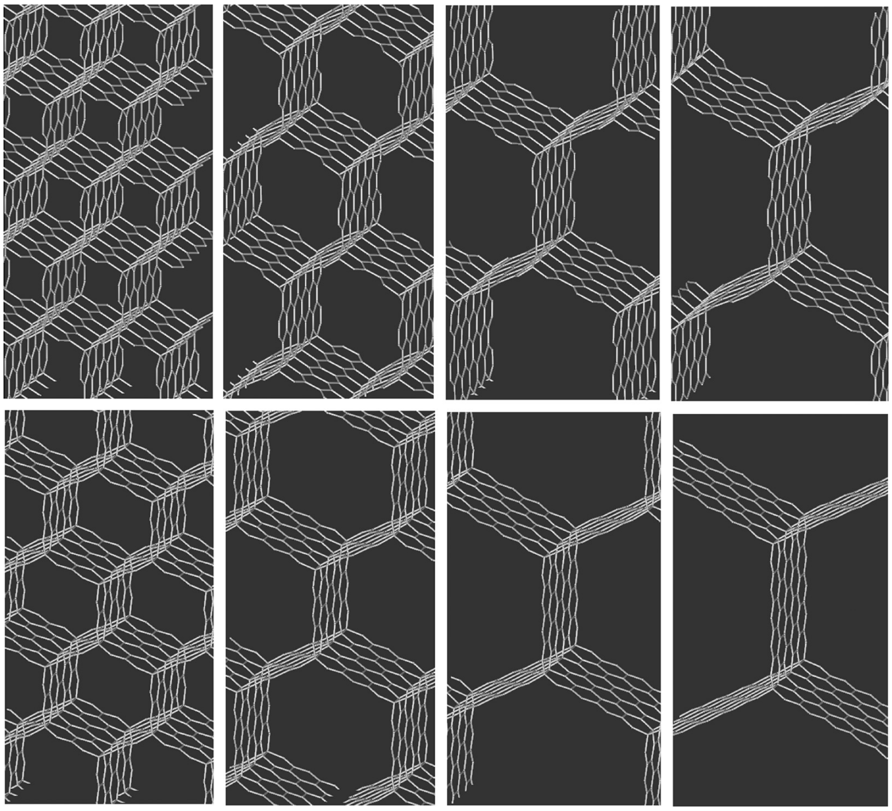

Figure 1. Armchair (top panels) and zigzag (bottom panels) symmetric carbon foams. From left to right, the structures of the (2,2), (3,3), (4,4), and (5,5) three-dimensional carbon networks are displayed.

tions,[21] quantum delocalization effects constitute the main factor leading to discrepancies with predictions based on classical methodologies. For structures with fairly narrow pores, quantum sieving can even prevent adsorption.[11]

The solution of the many-body problem, where significant quantum effects are present, remains as a challenging task for both theoretical and computational physics. At present, the numerical implementations of the path integral formalism of Feynman, e.g., path integral Monte Carlo (PIMC) and path integral molecular dynamics (PIMD) methods, constitute the standard techniques to make predictions on equilibrium properties of quantum many-body systems. They are based on the isomorphism between the partition function of a quantum particle and that of a classical ring polymer of P beads. Such mapping enables the use of the tools of classical statistical mechanics to obtain very accurate information on the thermodynamic properties of quantum systems (within statistical errors), since the exact quantum mechanical representation is recovered in the limit that P tends to infinity. Nevertheless, the computational cost of PIMC and PIMD calculations grows very fast for large values of P. Therefore, in many situations, less demanding alternatives not implying a significant loss of accuracy are highly desirable.

Density functional theory (DFT) is among these alternative techniques to calculate thermophysical properties of condensed phase systems. Being successfully applied to the study of classical fluids for a long time, in recent years, DFT has also been employed in the investigations of quantum systems. Implementations exploit the path integral isomorphism[22−28] and Mermin-like functionals.[29−36] However, most of these works addressed the properties of low temperature helium and applications to the hydrogen adsorption problem demonstrated that the proposed methodologies were not accurate enough to study the behavior of confined fluids.[28]

The purpose of this paper is to present numerically converged calculations of hydrogen physisorption on model nanofoams. The approach explicitly incorporates intermolecular interactions through a density functional theory for quantum fluids.[37] Several carbon foam arrangements have been chosen as target systems: zigzag and armchair (n,n), $n = 2−5$. Carbon foams are sponge-like carbon materials with attractive mechanical, thermal, and electrical properties.[38−42] The low mass density and high porosity of the symmetric models analyzed in this work make these carbon allotropes interesting as hydrogen storage media. In fact, as will be shown below, high storage capacities are predicted for these systems when the forces between hydrogen molecules are neglected. Therefore, it is worth evaluating the modification of their adsorption properties upon inclusion of the $H_2−H_2$ intermolecular interactions.

The paper is organized as follows. The main characteristics of the nanoporous hosts investigated are presented in section II. In section III, the theoretical methodology employed to evaluate adsorption capacities and the relevant intermolecular interactions are described, and numerical details are given in section IV. In section V, the results concerning the thermodynamic properties of the fluid physisorbed on each carbon foam, together with the microscopic density profiles, are presented and discussed. Finally, in section VI, conclusions are drawn.

II. FOAM STRUCTURES

Carbon foams are hypothetical carbon allotropes built from graphite-like segments (sp^2 carbons) linked by sp^3 carbon atoms. The resulting porous structures were first suggested in the 1990s,[43,44] and some of them have been theoretically investigated.[45−48] The synthesis of these foams has also attracted much attention[49,50] due to their potential applications in several areas such as thermal insulation, electrode manufacturing, catalyst supports, size-selective separation, etc. In general, these are lightweight materials with large surface areas, high thermal and electrical conductivities, and high mechanical strength. Their physical properties can be tuned over relatively wide ranges, according to the precursor and the production techniques used.[51−53]

Figure 1 displays the geometrical structures investigated in this work. It can be seen that graphene planes are assembled rigidly with one another at 120°, the junction being formed by sp^3-bonded atoms. In analogy with the nomenclature of carbon nanotubes, the two types of 3D carbon networks that can be constructed in this way are named as armchair and zigzag foams, depending on the pattern of the edges. The pore size is defined by the two indices (n,m), indicating the number of hexagonal rings between the junctions. These model foams present stable and covalent periodic structures. The stability of different types of carbon foams is discussed in detail elsewhere.[48] As hydrogen storage media, these systems offer the advantage that the pore size may be optimized via variation of the number of hexagons on each wall, so that larger hydrogen concentrations can be achieved. On the other hand, carbon foams have lower mass density than bundles of nanotubes of the same cavity diameters, which may lead to higher gravimetric storage capacities. Although the carbon foams synthesized so far are not single-walled, structures similar to the model ones analyzed in this work can be obtained experimentally.[49,50]

For the symmetric foams (n,n), zigzag and armchair, illustrated in Figure 1, an effective pore radius r_{eff} can be defined as the radius of the cylinder inscribed into the pore. The estimated values of r_{eff} for the carbon foams studied in this work are listed in Table 1. It should be noticed that the values of r_{eff} of (n,n) zigzag and $(n+1,n+1)$ armchair foams are very similar.

Table 1. Estimation of the Effective Radius for Different Foam Structures

radius (Å)	structure	
3.306	(2,2)	armchair
4.688	(2,2)	zigzag
5.220	(3,3)	armchair
6.870	(3,3)	zigzag
7.101	(4,4)	armchair
8.894	(4,4)	zigzag
9.031	(5,5)	armchair
11.178	(5,5)	zigzag

III. METHODOLOGY

A. Density Functional Theory. Both atomistic grand canonical Monte Carlo computer simulations[54−62] and density functional calculations[21,26,28] have stressed the role played by quantum effects on hydrogen physisorption and diffusion. In particular, the fully classical treatment of the H_2 translational degrees of freedom leads to an overestimation of the total H_2 uptakes by 3% at $T = 298$ K and 19% at $T = 77$ K for carbon foams produced via nanotube welding.[63,64] Albeit most of these calculations employ the second-order semiclassical Feynman−Hibbs approximation of the density matrix, their results are indicative of the magnitude of quantum delocalization effects in the confined hydrogen fluid. For the present study, we employ the quantized liquid DFT (QLDFT) approach introduced in ref 37. This approach is based on a linear-scaling density matrix algorithm, which has been shown to produce identical results to direct diagonalization for matching choices of the real-space grid spacing and kinetic cutoff.[65] For the computation of thermodynamic properties in the grand canonical ensemble, at constant V, temperature T, and chemical potential μ, a reference system of noninteracting particles obeying Bose−Einstein statistics is introduced.[21] It should be noticed that, in spite of the bosonic nature of H_2 molecules, this feature has been shown to play a minor role at temperatures of interest for hydrogen storage. Nevertheless, above liquid nitrogen temperature, the storage requirements and the computational cost of evaluating the partition function and the particle density of the Bose−Einstein and Boltzmann fluids are nearly the same. Hence, all the results presented in the next section have been calculated using a series expansion of the Bose−Einstein distribution function:[21]

$$\begin{aligned}\hat{\rho}_s &= \frac{1}{e^{\beta(\hat{H}_s-\mu)}-1}\\ &= \sum_{k=1}^{\infty} e^{-k\beta(\hat{H}_s-\mu)}\\ &= \sum_{k=1}^{\infty}\sum_{m=0}^{\infty}\frac{[-k\beta(\hat{H}_s-\mu)]^m}{m!}\end{aligned} \tag{1}$$

where $\beta = 1/k_B T$ is the inverse temperature and $\hat{H}_s$ is the effective Hamiltonian operator of the reference fluid.

$$\begin{aligned}\hat{H}_s = &-\frac{\hbar^2}{2M_{H_2}}\nabla^2 + v_{\mathrm{ext}}(\mathbf{r}) + \int v_{12}(|\mathbf{r}-\mathbf{r}'|)\rho(\mathbf{r}')\,\mathrm{d}^3\mathbf{r}'\\ &+ v_{\mathrm{xc}}[\rho]\end{aligned} \tag{2}$$

where M_{H_2} is the mass of hydrogen molecules, $\rho(\mathbf{r})$ is the H_2 density (normalized to the number of particles N), v_{12} represents the interaction potential between H_2 molecules, and $v_{\mathrm{ext}}(\mathbf{r})$ is the external field of the host system. Within this *ansatz*, the grand potential of the interacting system

$$\begin{aligned}\Omega[\rho] = \Omega_s[\rho] &- \frac{1}{2}\iint \rho(\mathbf{r})\rho(\mathbf{r}')v_{12}(|\mathbf{r}-\mathbf{r}'|)\,\mathrm{d}^3\mathbf{r}\,\mathrm{d}^3\mathbf{r}'\\ &- \int \rho(\mathbf{r})v_{\mathrm{xc}}(\mathbf{r})\,\mathrm{d}^3\mathbf{r} + F_{\mathrm{xc}}[\rho]\end{aligned} \tag{3}$$

is written in terms of the grand potential of the reference fluid

$$\hat{\Omega}_s = -\frac{1}{\beta}\log Z_s = -\frac{1}{\beta}\sum_{k=1}^{\infty}\sum_{m=0}^{\infty}k^{m-1}\frac{[-\beta(\hat{H}_s-\mu)]^m}{m!} \tag{4}$$

and the exchange-correlation contribution F_{xc}. The second and third terms in eq 3 are introduced in order to avoid double counting of the Hartree-like interaction energy and to cancel the contribution due to the exchange-correlation potential v_{xc}. The latter is derived within the local density approximation (LDA)

$$v_{\mathrm{xc}}(\mathbf{r}) = \epsilon_{\mathrm{xc}}[\rho(\mathbf{r})] + \rho(\mathbf{r})\frac{\delta\epsilon_{\mathrm{xc}}}{\delta\rho(\mathbf{r})} \tag{5}$$

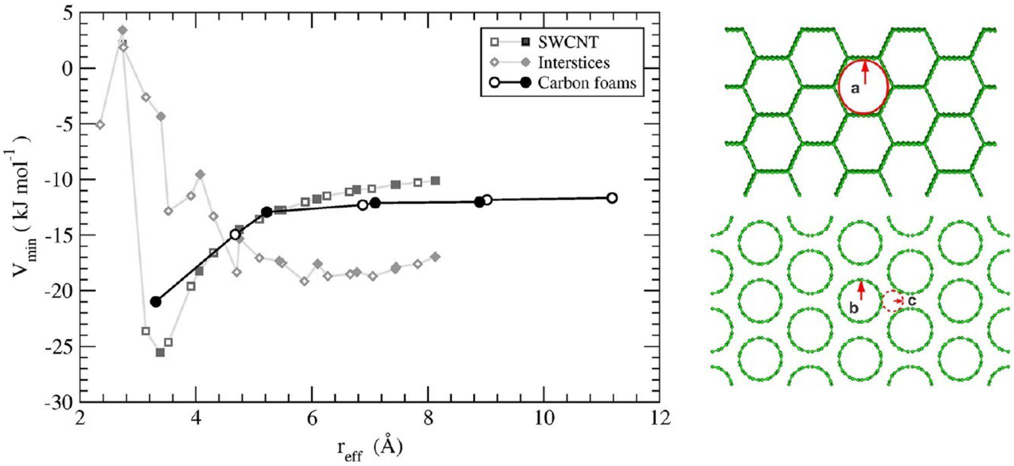

Figure 2. Changes of the minima of the H_2-host interaction potential with the radius of the channels in carbon foams (circles). The well depths of the adsorption potential inside single-walled carbon nanotubes (squares) and in nanotube bundle interstitial channels (diamonds) are also shown. Filled and empty symbols correspond, respectively, to the armchair and zigzag types of arrangements. The effective pore radii for foams (a) and for the inner (b) and interstitial (c) spaces of nanotube bundles are illustrated on the right. The graphical representations correspond to the (3,3) zigzag carbon foams and the (7,7) armchair nanotubes.

with the exchange-correlation energy density given by

$$\epsilon_{xc}[\rho] = \frac{F_{expt}[\rho, T]}{N} + \frac{1}{\beta}\log\left(\frac{Z_{kin}}{\rho V}\right) - \frac{\rho}{2}\int v_{12}(|\mathbf{r} - \mathbf{r}'|)\, d^3\mathbf{r}' \qquad (6)$$

$F_{expt}[\rho,T]$ is the free energy of the corresponding uniform fluid, which is taken from thermodynamic data based on an empirical equation of state for hydrogen,[66] while Z_{kin} is the one-particle canonical partition function in the free space. The empirical equation of state holds for pressures up to 2 GPa, which constitutes a broad enough range for the investigation of hydrogen physisorption on carbon substrates.

The molecular density $\rho(\mathbf{r})$ is given by the diagonal elements of the number operator $\hat{\rho}_s$, evaluated using a three-dimensional finite-difference representation of the effective Hamiltonian $\hat{H}_s$. Once the distribution $\rho(\mathbf{r})$ is known, the average concentration n_{ads} of the physisorbed molecules, the equilibrium constant K_e, and the gravimetric storage gw capacity can be computed:

$$n_{ads} = \frac{1}{V}\int \rho(\mathbf{r})\, d^3\mathbf{r} \qquad (7)$$

$$K_e = n_{ads}/n \qquad (8)$$

$$gw(\%) = \frac{100 \cdot n_{ads}}{n_{ads} + \frac{M_C}{M_{H_2}} n_C} \qquad (9)$$

where n is the density of the external gas, while M_C and n_C represent the mass of a carbon atom and the number density of carbon atoms in the host structure, respectively.

This is, as we will show later, a significant improvement over the simplified treatment, the fugacity-corrected ideal gas approximation (FCIGA), that has been previously employed to evaluate the adsorption isotherms and the storage capacities of graphene, slit pores, and C_{60} intercalated graphene.[67,69] The computation was made by solving the time-independent Schrödinger equation for a single H_2 particle with the Hamiltonian

$$\hat{H} = -\frac{\hbar^2}{2M_{H_2}}\nabla^2 + v_{ext}(\mathbf{r}) \qquad (10)$$

employing the same three-dimensional grid as in QLDFT calculations. The procedure is augmented by an estimation of the nonideality of the guest fluid, valid for slowly varying confinement potentials (within the characteristic interparticle distances).[65] The empirical correction proceeds as follows:

(i) The equilibrium constant $K_e = Z_{ads}/Z_{kin}$ is calculated from the partition functions of the adsorbed (Z_{ads}) and free (Z_{kin}) fluids. The latter have been obtained by evaluating the single-particle energies on the grid, using the same numerical approximations.

(ii) For a given external pressure p, the "internal" pressure p_{int} is calculated after the formula $p_{int} = K_e p$. The volumetric and gravimetric capacities are evaluated by inserting the values of the internal pressure and the temperature in the empirical equation of state.

The comparison between the results of QLDFT calculations and those obtained via the FCIGA allows the relevance of the explicit inclusion of H_2−H_2 interactions to be evaluated and the range of validity of the empirical correction to be established.

B. Potential Energy Surface. For the calculation of the relevant adsorption and thermodynamic properties, a detailed knowledge of the interaction of guest molecules and the host structure is necessary. The interaction potential $v_{ext}(\mathbf{r})$ between carbon atoms and hydrogen molecules is represented as a superposition of carbon−H_2 pair potentials

$$v_{ext}(\mathbf{r}) = \sum_i A e^{-a|\mathbf{r}-\mathbf{r}_i|} - \frac{C}{|\mathbf{r} - \mathbf{r}_i|^6} \qquad (11)$$

where $\mathbf{r}_i$ are the positions of carbon atoms in the steady carbon structure. The attractive singularity of this functional form is avoided by capping each term at 120 kJ mol^{-1}, corresponding to a carbon−H_2 separation of 1.8 Å. Potential parameters were taken from the literature.[67,68] The advantages of this type of potentials are discussed in ref 67, where a detailed comparison with Lennard-Jones types has been performed.

In the evaluation of v_{ext}, we take into account the contribution of three additional unit cells along each direction.

The inclusion of further replicas of the unit cell does not appreciably modify $v_{\text{ext}}(\mathbf{r})$.

The use of the potential energy surface in the form of eq 11 provides a unique description of the hydrogen−host interaction for the different carbonaceous media within the same framework. Furthermore, it prevents the uncertainties in the evaluation of hydrogen physisorption arising from the use of empirical potential functions. A comparison between the minima of the external potentials v_{ext} inside carbon foams, single-walled carbon nanotubes, and the interstitial space in nanotube bundles is shown in Figure 2. The well depths are plotted as a function of the radii of the channels. An interesting result is that the minima of the surface−H_2 interaction potential are nearly constant for carbon foams with pore radii larger than 7 Å. A closer look into the arrangement of the carbon atoms gives a better understanding of this behavior: the radius increases with the number of rings forming the cavity walls; however, the coordination and the bond angles of the sp^3 carbon atoms remain the same. The contribution to the interaction potential in the region of the sp^3 carbon atoms is given by the overlapping potentials of atoms located around the corners. Since the enlargement of the cavity does not influence the geometry and the number of C atoms in the vicinity of the corners, the interaction potential on these sites is nearly constant. The main adsorption sites are precisely located in these regions, close to the intersections between the walls of the channels (see Figure 2). On the other hand, the potential in the middle of the channel becomes weaker as the radius gets larger. This is similar to the potential inside of the carbon nanotubes (see, for example, ref 54).

In this study, hydrogen molecules are regarded as featureless particles, so v_{12} depends only on the intermolecular separation. The H_2−H_2 interaction is modeled through a Morse function

$$v_{12}(r) = D[e^{-2\alpha(r-r_e)} - 2e^{-\alpha(r-r_e)}] \tag{12}$$

with parameters $D = 0.291$ kJ mol^{-1}, $r_e = 3.511$ Å, and $\alpha = 1.592$ Å^{-1}. The potential parameters were obtained from the fit of the isotropic average of *ab initio* calculations of the intermolecular potential energy surface.[70]

Upon inclusion of the carbon−hydrogen, hydrogen−hydrogen, and exchange-correlation contributions in the total potential energy, a cutoff of 42 kJ mol^{-1} above the global minimum was introduced in order to improve the numerical stability of the algorithm (for details, see ref 37).

IV. COMPUTATIONAL DETAILS

The hydrogen physisorption on armchair and zigzag carbon foams has been studied in a broad range of thermodynamic conditions, relevant for practical applications. We considered temperatures from the nitrogen condensation point ($T_{\min} = 77$ K) to $T_{\max} = 450$ K and a range of external gas concentrations between a dilute gas ($n_{\min} = 5.4 \times 10^{-4}$ kg/m^3, corresponding to a molar volume $v_m = 3.74$ m^3) and the density $n_{\max} = 55.6$ kg/m^3 ($v_m = 36.2$ cm^3). As the exchange-correlation potential and its contribution to the free energy, the chemical potential μ is retrieved, for every external gas pressure p and temperature T, from the experimental data of the homogeneous fluid:

$$\mu = \frac{F_{\text{expt}}(p, T)}{N} + \frac{p}{n} \tag{13}$$

As stated above, the matrix elements of the occupation number operator $\hat{\rho}_s$ are calculated via the formal power expansion (1) by introducing a finite-difference representation of the Hamiltonian in a three-dimensional grid. The number of points in the uniform mesh was varied in order to keep the coarsest grid spacing along each of the Cartesian axis below 0.4 Å. This choice is found to yield converged results. The resulting Hamiltonians have dimensions between ∼8000, for the (2,2) armchair structure, and ∼60000, for the (5,5) zigzag arrangement. However, this representation is very sparse.[65] The linear algebra operations needed to evaluate $\hat{\rho}_s$ are handled according to the implementation discussed in refs 65 and 37. The canonical kinetic partition function Z_{kin} was obtained by explicitly evaluating the eigenvalues of the Schrödinger equation for a free particle of mass M_{H_2} on the 3D grid. The QLDFT set of eqs 1, 5, 6, and 2 is solved self-consistently by damped stationary point iterations

$$\rho^{(i)}(\mathbf{r}) = \lambda\rho^{(i)}(\mathbf{r}) + (1-\lambda)\rho^{(i-1)}(\mathbf{r}) \tag{14}$$

$$v_{\text{eff}}^{(i)}(\mathbf{r}) = \lambda v_{\text{eff}}^{(i)}(\mathbf{r}) + (1-\lambda)v_{\text{eff}}^{(i-1)}(\mathbf{r}) \tag{15}$$

with a mixing coefficient of $\lambda = 0.15$. Iterations start from the density field $\rho_{\text{clas}}(\mathbf{r})$ predicted by the classical liquid density functional theory for the same external potential.[21] The series (1) and (4) were cut at $k_{\max} = 5$ and $m_{\max} = 50$, since those terms were sufficient to achieve convergence in the whole range of temperatures and pressures considered. At every step, matrix elements smaller than 10^{-4} times the largest value were neglected in the computation of $\hat{\rho}_s$.

V. RESULTS AND DISCUSSION

A. Adsorption Isotherms.

In the QLDFT approach, the calculations are done for a given set of temperatures T and concentrations n_{ads} as inputs, whereas the chemical potential $\mu(n_{\text{ads}},T)$ and external matching pressure $p = p(\mu,T)$ are obtained as outputs. Performing such calculations for a set of T,n_{ads} pairs, the results are then represented in the form of isotherms $n_{\text{ads}}(p,T)$. The density of adsorbed molecules is indicative of the hydrogen volumetric storage capacity, measured in kg/m^3, or it is converted in the gravimetric capacity, given in percentage. On the other hand, approximate values of the volumetric capacity (based on ideal gas calculations) are extracted directly from the empirical equation of state. Albeit being unrealistic at intermediate and large densities, these ideal gas calculations provide an assessment of single-particle quantum effects triggered by the structure.

In Figure 3, the values of the difference ΔF between the free energy of a single adsorbed H_2 molecule with respect to a free one are represented, for several temperatures, as a function of the honeycomb cell radius. ΔF gives the strength of the H_2 binding to the material. Therefore, it provides a direct indication of the relative abilities of the different nanostructures to naturally adsorb hydrogen gas and of how the H_2 density in the material will deplete with the increase of the thermal energy. For carbon foams, the binding energies ΔF are larger than for graphene layers at the same temperature but smaller than for carbon nanotubes. At room temperature, our calculations suggest a maximum of the H_2-host free energy of approximately 12 kJ mol^{-1}, for a channel radius of 3.3 Å. Increasing the radius up to 11.2 Å causes the interaction to drop down to around 3.8 kJ mol^{-1}. It can be noticed that lowering the temperature from $T_{\max} = 450$ K down to $T_{\min} = 77$ K leads to an increase of the binding free energy by a factor of 2 for (2,2) armchair graphitic foams. For a given temperature, the

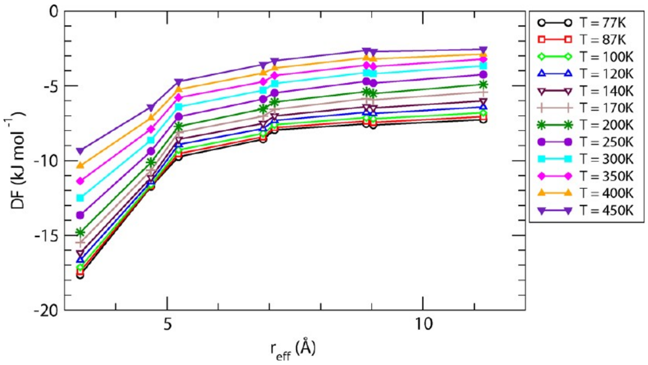

Figure 3. Binding free energies ΔF, evaluated within the independent-particle model, as a function of the honeycomb cell radius for temperatures in the range T_{min} = 77 K and T_{max} = 450 K.

energies ΔF grow monotonically with the increase of the pore diameter; i.e., ΔF is very sensitive to the size of the cavity only for small pores ($r_{eff} < 8$ Å). Therefore, for the storage capacities, calculated within the ideal gas approximation, a strong dependence on the radius of the smaller cavities can be expected. At intermediate and high guest densities, this picture has to be corrected by the explicit inclusion of the H_2−H_2 interaction.

A comparison between the adsorbed hydrogen concentrations, evaluated using the QLDFT and the independent-particle models as a function of the foam channel radii, is shown in Figure 4. The average molecular densities were computed at external gas pressures p_1 = 50 bar and p_2 = 100 bar. At moderate external pressures, the FCIGA is insufficient to describe the physisorption process. For temperatures $T \leq$ 200 K, the volumetric storage capacities of all the carbon foams considered in this work fulfill the present US DoE target for automotive applications (40 kg/m^3).[14] However, an important fraction of these large adsorption densities lies outside the range of validity of the empirical equation of state[66] that has been employed as reference in the excess functional; i.e., they correspond to pressures above 2 GPa. Above room temperature, this simple treatment is capable of predicting guest densities in qualitative agreement with QLDFT results for the larger carbon foams, i.e., for those adsorption potentials which vary slowly within the characteristic length-scale of the intermolecular forces. For the larger pores, the noninteracting model also reflects the correct dependence of the volumetric capacity with respect to the cavity size. The most important deviations between the two types of calculations arise for small channels. As a consequence of the strongest binding potentials, a significantly enhanced molecular concentration is obtained, if the two-particle interaction energy is neglected. Within FCIGA, the local density around the main adsorption sites may even exceed the close-packing limit. On the contrary, for the real hydrogen fluid, the increase of the local density inside narrow pores, due to the larger substrate−H_2 van der Waals attraction, causes also an enhancement of the H_2−H_2 repulsion forces. Hence, the optimum hydrogen storage properties in these materials arise from the competition between the strength of the surface−H_2 attraction and the accessible volume to minimize the intermolecular repulsion.

The limited range of validity of the real gas correction employing fugacities becomes apparent by examining the overall behavior of the equilibrium constant K_e as a function of pressure and temperature. As shown in Figure 5 for a (5,5)

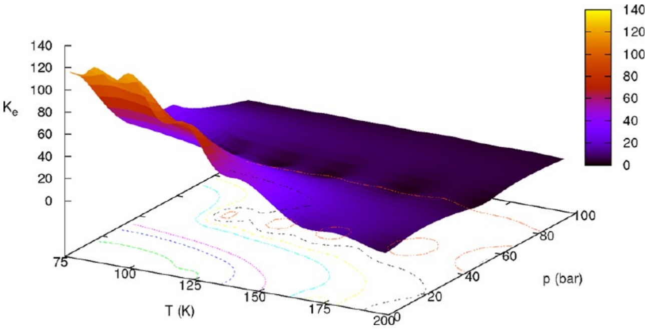

Figure 5. Equilibrium constant K_e for the physisorption of molecular hydrogen inside (5,5) zigzag carbon foams as a function of the temperature T and of the external gas pressure p.

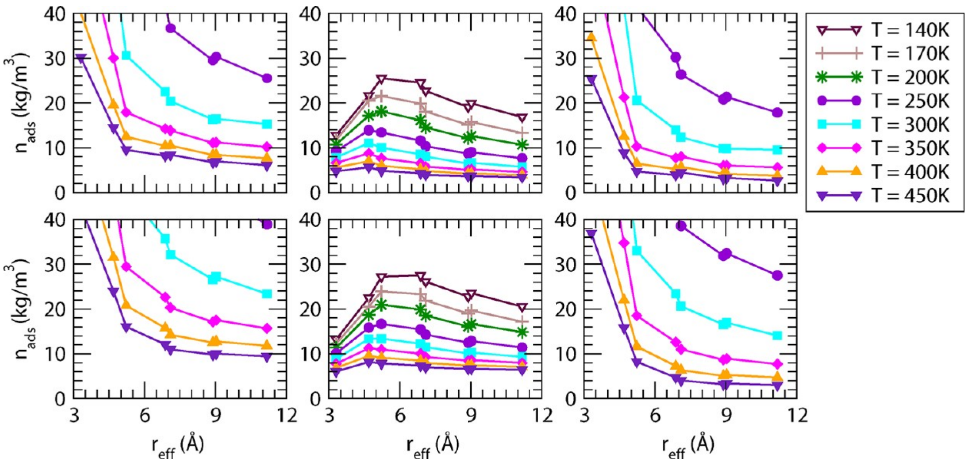

Figure 4. Volumetric storage capacities for graphitic foams, plotted against their channel radii, for external gas pressures p = 50 bar (top) and p = 100 bar (bottom). For both pressures, the left panels correspond to the adsorbed hydrogen density estimated within the independent-particle model, while the middle panels show the H_2 uptake calculated via QLDFT. Different symbols correspond to the average molecular concentrations predicted at selected temperatures in the range between 140 and 450 K. The differences between the densities of adsorbed H_2, calculated using these two methods, are shown in the right panels.

zigzag carbon foam, K_e exhibits a marked dependence on both p and T. Therefore, the "internal" pressure, corresponding to specific values of the thermodynamic variables of the external hydrogen gas, can only be estimated from nearby points on the p,T plane. The values of K_e, calculated by solving the time-independent Schrödinger equation for a single H_2 particle, correspond to the low pressure limit in Figure 5. As a consequence, the equilibrium constants of the independent-particle model overestimate those of the interacting fluid, leading to flawed estimations of p_{int} and of the volumetric storage capacity.

A typical example of QLDFT isotherms is given in Figure 6, where the volumetric capacity is shown as a function of the external gas pressure for two selected structures: (2,2) armchair (r_{eff} ~3.3 Å) and (5,5) armchair (r_{eff} ~8.9 Å). These two carbon foams represent two extreme cases of arrangements of the same symmetry.

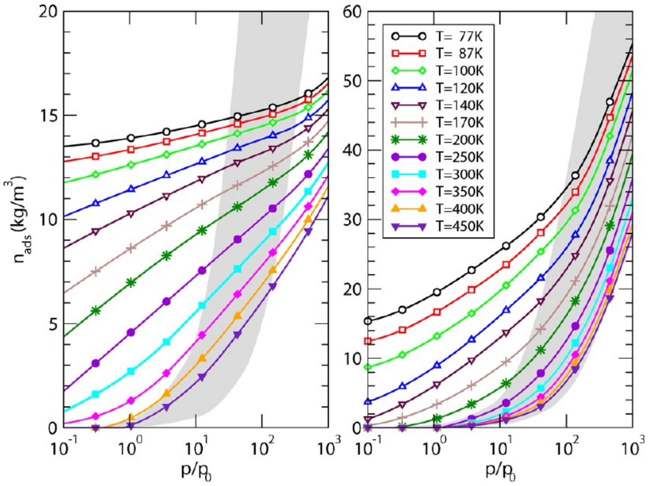

Figure 6. Computed adsorption isotherms $n_{ads}(p, T)$ as a function of the pressure p of the external gas at fixed temperatures T in the range T_{min} = 77 K and T_{max} = 450 K. The evaluated adsorption isotherms in the left and right panels correspond to the (2,2) and (5,5) armchair carbon foams, respectively. The gray areas show the isotherms of the homogeneous external gas for the same range of temperatures.

In order to appreciate the influence of the structure on the storage capacity, we also plot the isotherms obtained for the free gas in the range of temperatures from T = 77 K to T = 450 K, shown as gray areas in Figure 6. The behavior of the molecular hydrogen in the small pore is found to be much more different from its free gas limit than in the case of the large pore structures. This is in agreement with the general understanding of the adsorption process: the more pronounced effects of the H_2-structure interaction on the storage capacity will be attained for the smaller pore sizes. In the case of carbon foams with narrow channels (left panel), the slope of the isotherms $n_{ads}(p,T)$ is smaller than in the case of wide channels (right panel). Thus, the dependence on pressure and temperature is weaker for foams with narrow channels. For low values of pressure 1 bar < p < 10 bar, except at very high temperatures, the presence of the foam will enhance hydrogen concentration. The comparison with the free gas isotherms shows that hydrogen cannot be stored efficiently in this material beyond ~15 kg/m^3 (at T = 77 K and p = 31 bar). At very low pressures (p ~0.1 bar) and above liquid nitrogen temperature, the density of adsorbed molecules will be larger for the smaller pores than for the (5,5) armchair foams (Figure 6, right panel). This is consistent with the fact that at such densities the independent-particle picture of physisorption is valid and the storage properties will be driven by the adsorption potential well depth. However, at high pressures, the storage capacity of the (5,5) armchair structure becomes higher. For this system, it is possible to reach H_2 concentrations up to 34 kg/m^3 at T = 77 K and p = 89 bar. In technological terms, this means that the effect of increasing pressure and decreasing temperature is more efficient in the case of large structures.

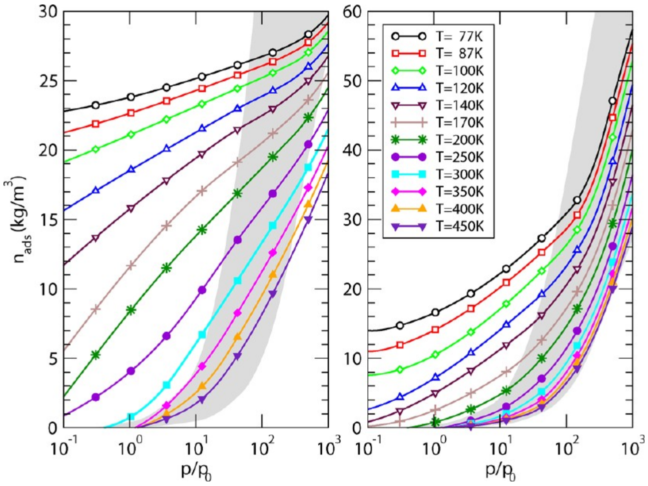

Figure 7. Computed adsorption isotherms $n_{ads}(p,T)$ as a function of the pressure p of the external gas at fixed temperatures T in the range T_{min} = 77 K and T_{max} = 450 K. The evaluated adsorption isotherms in the left and right panels correspond to the (2,2) and (5,5) zigzag carbon foams, respectively. The gray areas show the isotherms of the homogeneous external gas for the same range of temperatures.

This conclusion is further reinforced by the adsorption isotherms computed for the set of (n,n) zigzag carbon foams. Figure 7 illustrates the pressure dependence of the volumetric capacity for the smallest (left panel, n = 2, r_{eff} ~4.7 Å) and the largest (right panel, n = 5, r_{eff} ~11.2 Å) zigzag structures. The total hydrogen uptake in the (2,2) zigzag foams depends more sensitively on the external gas pressure than the (2,2) armchair arrangement. Moreover, higher hydrogen concentrations can be achieved in the zigzag 3D carbon network, amounting to 26 kg/m^3 at T = 77 K and p = 63 bar. At low and intermediate pressures (p < 100 bar) and T < 200 K, the slopes of the isotherms increase as the external pressure gets larger. On the contrary, above T = 200 K, the slopes generally decrease as p is augmented. In a similar way, in the case of (2,2) armchair structures, the variation of the slopes with the increase of the external pressure is different below and above T = 250 K. For both structures, the transition temperatures correspond to thermal energies which are approximately 0.1 times the potential well depth at the main adsorption sites. This temperature dependence, which appears only for the two extreme confinement potentials, suggests that this behavior is caused by the emergence of quantum delocalization effects. In fact, the influence of quantum effects on hydrogen adsorption in the smallest carbon foams has been stressed by calculations carried out within quantized and classical liquid density functional theories.[21] The $n_{ads}(p,T)$ curves for the (5,5) zigzag foams closely follow those obtained for the (5,5) armchair structure. At low temperatures, the molecular density is slightly lower in the former case. This feature indicates that the increase of the effective pore radius from 8.9 to 11.2 Å does not have a significant influence on the amount of physisorbed H_2. It is a consequence of the similarities of the adsorption potentials inside both cavities.

Summing up, while the adsorption properties of (2,2) armchair foams are noticeably different from those of the (2,2) zigzag arrangements, the volumetric storage capacities of the (5,5) armchair and zigzag structures are pretty close. A closer look into the effective potential $v_{\mathrm{eff}}(\mathbf{r})$ inside the unit cells of these four carbon frameworks gives a more clear picture of this behavior. The contour plots of $v_{\mathrm{eff}}(\mathbf{r})$, evaluated at $T = 77$ K and $p = 100$ bar, are displayed in Figure 8. At moderate external pressures, after adding the exchange-correlation contribution, the minima of the potential $v_{\mathrm{eff}}(\mathbf{r})$ are very similar for all the structures (approximately −3.9 and −3.8 kJ mol^{-1} for the (2,2) and (5,5) carbon foams). In the (2,2) pores (Figure 8a and c), this strength of the H_2-host interaction potential reduces to ≈ -3.4 kJ mol^{-1} at the center of the cavity. Since the range of variation of the effective potential in the (2,2) armchair and zigzag carbon foams is nearly the same, the enhanced adsorption capacity of the latter is a consequence of its larger accessible volume. The extreme values of $v_{\mathrm{eff}}(\mathbf{r})$ are also very similar for the (5,5) armchair and zigzag foams. In Figure 8b and d, the adsorption regions are parallel to the channel walls. The interaction strength decreases faster with the distance to the graphenic planes for the zigzag structures than for armchair structures, leading to slightly smaller average molecular densities.

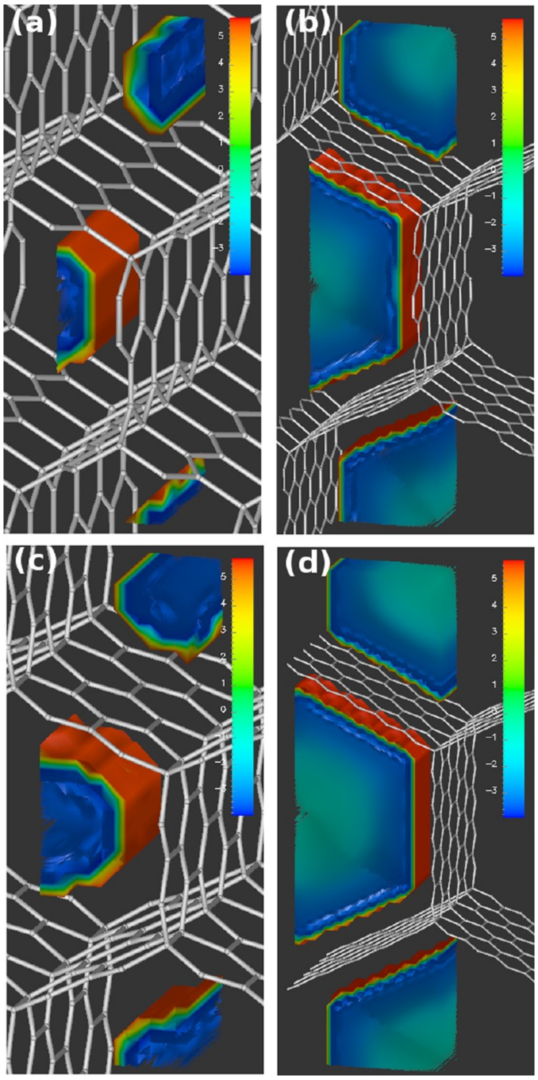

Figure 8. Effective potential energy isosurfaces inside the unit cells of (a) (2,2) armchair, (b) (5,5) armchair, (c) (2,2) zigzag, and (d) (5,5) zigzag carbon foams at temperature $T = 77$ K and external gas pressure $p = 100$ bar. The isosurfaces cover the range from −3.9 to 5.8 kJ·mol^{-1}. Cavity sizes have been scaled to allow a better visualization of the overall shape of the effective potential.

The dependence on the pore radius of carbon foams of the gravimetric capacity is shown in Figure 9. The $gw(r_{\mathrm{eff}})$ curves are given for temperatures 77 K < T < 450 K and pressures $p_{\mathrm{low}} = 5$ bar (left panel) and $p_{\mathrm{high}} = 100$ bar (right panel). The external gas pressure p_{low} is representative for the low coverage regime. On the other hand, p_{high} roughly corresponds to the highest external pressures at which the host materials retain positive excess storage capacities. At 5 bar, the gravimetric capacities exhibit weak maxima. These modest peaks correspond to different nanostructures: the highest value of gw is reached for the (4,4) armchair structure at $T \leq 100$ K; at $T = 120$ K, the largest gravimetric storage capacity is achieved for the (3,3) zigzag foam; at $T = 140$ K and $T = 170$ K, the maximum occurs for the (3,3) armchair material and so on. In summary, the maximum of gw is shifted to the systems having narrower pores as the temperature is increased. This trend reflects the role of quantum delocalization effects on adsorption. For high enough temperatures, classical adsorption theory is valid and the number of molecules attached to the surface will be determined by the strength of the guest−host interaction, which is maximal for the smallest graphitic foams. Likewise, at $p_{\mathrm{high}} = 100$ bar, the gravimetric storage capacity increases monotonically with the pore radius for all temperatures considered. Since the adsorbed density decreases as the size of the cavity gets larger (for channels with $r_{\mathrm{eff}} > 6$ Å), it is evident that the higher gravimetric capacities are attained at the expense of the lower mass densities of the carbon structures with larger pores. For the (5,5) zigzag carbon foam at $T = 77$ K, the weight of the physisorbed fluid represents 4.5% of the total mass. This value is similar to the recently reported experimental values for physical adsorption capacities on carbon surfaces,[9] although it is still lower than the US DoE requirements for mobile applications.

B. Microscopic Density Profiles. To characterize the microscopic structure of the adsorbed fluid, we evaluated the ratio between the pressure p_{max} corresponding, according to the empirical equation of state,[66] to the maximum local density of hydrogen molecules inside the cavity and the external pressure p. The magnitude p_{max}/p measures the capability of the structure to create large density peaks, which is directly related to the ability of the material to adsorb hydrogen. The ratios p_{max}/p (logarithmic scale) for selected pressures ($p = 5$, 50, and 100 bar), at room temperature and at liquid nitrogen temperature, are summarized in Table 2. At low temperatures, the carbon foams act as nanopumps, creating highly structured density profiles, characterized by large ratios p_{max}/p. The pressures matching the local maxima of the hydrogen density are between $\sim 10^2$ and $\sim 10^4$ times that of the external gas. As the temperature goes up, this capability is dramatically reduced. At room temperature, the variation of p_{max}/p gets considerably smaller: p_{max} varies from ~ 20 to ~ 500 times the external pressure. The comparison among the different nanostructures

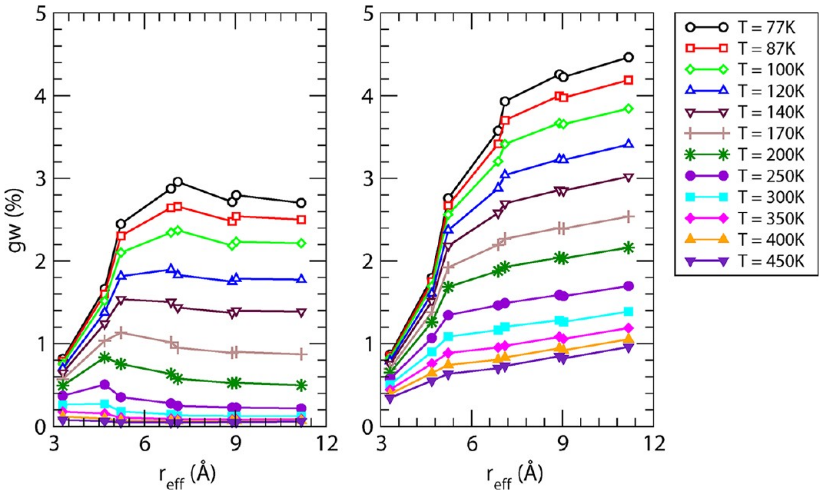

Figure 9. Gravimetric storage capacities *gw* as a function of the foams' effective pore radii r_{eff}, at pressures p_{low} = 5 bar (left panel) and p_{high} = 100 bar (right panel), for temperatures in the range T_{min} = 77 K and T_{max} = 450 K.

Table 2. Logarithm of the Nanopump Efficiency, $\log_{10}(p_{\mathrm{max}}/p)$, for Different Foams, as a Function of Their Effective Radius, r_{eff}, for Selected External Gas Pressures (p = 5, 50, and 100 bar) and Temperatures (T = 77 and 300 K)

r_{eff} (Å)	p = 5 bar	p = 50 bar	p = 100 bar
	T = 77 K		
3.306	4.252	3.389	2.428
4.688	4.008	3.138	2.173
5.220	3.924	2.998	1.969
6.870	3.883	2.928	1.868
7.101	3.859	2.951	1.942
8.894	3.871	2.933	1.890
9.031	3.846	2.922	1.896
11.178	3.829	2.882	1.830
	T = 300 K		
3.306	2.674	1.910	1.856
4.688	2.087	1.597	1.528
5.220	1.815	1.449	1.379
6.870	1.730	1.402	1.331
7.101	1.690	1.400	1.320
8.894	1.699	1.385	1.314
9.031	1.661	1.366	1.293
11.178	1.630	1.346	1.273

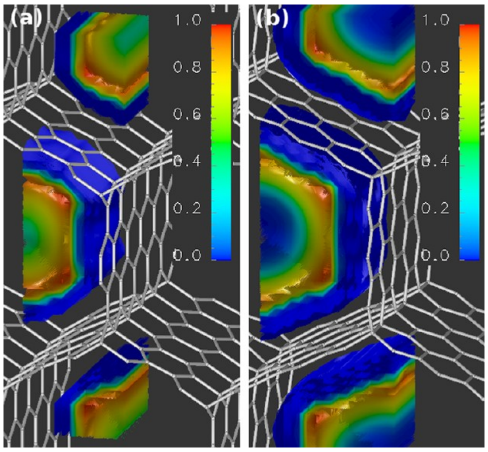

Figure 10. Spatial distribution of physisorbed hydrogen at external gas pressure p = 1 bar and temperature T = 77 K, inside the unit cell of (3,3) armchair (left panel) and (3,3) zigzag (right panel) carbon foams, shown by means of constant H_2 density surfaces. The color scale is normalized to the height of the main peak of molecular distribution.

shows that there is also a relatively weak dependence of this nanopump efficiency on the pore size. At p = 5 bar and T = 77 K, the largest density $\rho(\mathbf{r})$ inside the (2,2) armchair network corresponds, for a homogeneous hydrogen gas, to a pressure of about 2.6 times larger than the corresponding value for the (5,5) zigzag carbon foam. The ratio p_{max}/p becomes 3.2 and 4 times larger for the (2,2) armchair, in comparison to the (5,5) zigzag honeycomb structure, at p = 50 bar and p = 100 bar, respectively.

The spatial distribution of the hydrogen molecules inside the unit cells of (3,3) armchair and zigzag carbon foams, at external pressure p = 1 bar and temperature T = 77 K, is shown in Figure 10. The density is delocalized along the channel walls, indicating free lateral motion of the molecules along the wall surfaces. This is in agreement with previous path-integral and Monte Carlo simulations of H_2 adsorption on graphite-like materials.[2,3,7] On the other hand, in the plane perpendicular to the channel axis, the density profile is highly inhomogeneous. It is characterized by a forbidden region for hydrogen adsorption close to the carbon walls and sharp density peaks around the main adsorption sites, decaying to approximately 0.3 ((3,3) armchair, Figure 10a) and 0.01 ((3,3) zigzag, Figure 10b) times the maximum concentration. It can be noticed that for the zigzag structures the principal adsorption sites are clearly defined. In the vicinity of these main peaks, the density reaches about 70% of the peak heights. However, the preferential adsorption sites in the (3,3) armchair unit cell are interconnected by a region, where the minimum concentration is above 90% of the largest density. This feature causes the total number of particles per unit volume to be slightly larger in the armchair network, but the lower mass density of the zigzag foams gives higher gravimetric storage capacities for the latter structures.

Moreover, Figure 11 illustrates the microscopic density profiles inside (4,4) armchair and zigzag foams. The diameter of the pores of the (4,4) armchair structure is 36% larger than that of the (3,3) armchair carbon foam. The constant density surfaces in Figure 11a show that the redistribution of hydrogen

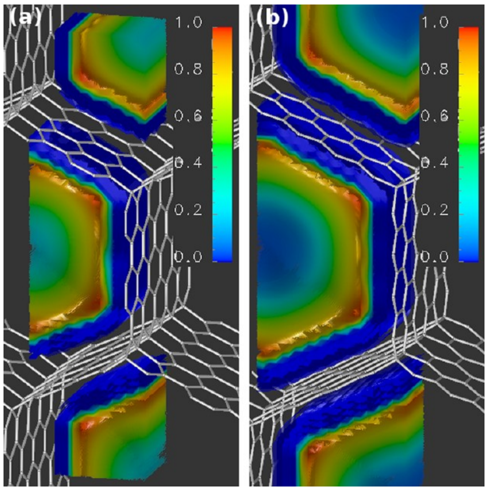

Figure 11. Spatial distribution of physisorbed hydrogen at external gas pressure p = 100 bar and temperature T = 77 K, inside the unit cell of (4,4) armchair (left panel) and (3,3) zigzag (right panel) carbon foams, shown by means of constant H_2 density surfaces. The color scale is normalized to the height of the main peak of molecular distribution.

molecules over the larger accessible volume is able to compensate the enhancement of H_2-H_2 repulsion caused by the increase of the external pressure. The molecular reorganization results in a more structured molecular distribution, compared to that of (3,3) armchair foams (see Figure 10a). The hydrogen molecules inside the (4,4) armchair cavity concentrate around individual adsorption sites, close to the corners, and the probability to find a H_2 molecule on the axis channel is ∼15% of the value at the minima of the adsorption potential. On the other hand, Figure 11b shows that molecular rearrangement also takes place for the (4,4) zigzag system. The pore radius of this material is 29% larger than that of the (3,3) zigzag. The density at the center of the (4,4) cavity is 0.03 times the height of the main adsorption peaks, showing that the enlargement of the volume is not enough to overcome the stronger intermolecular repulsion. The integrated densities yield volumetric and gravimetric storage capacities of ∼24 kg/m^3 and ∼4.2%, respectively.

VI. CONCLUSIONS

The adsorption properties of model nanostructured materials have been investigated for broad ranges of external gas pressures and temperatures. The density functional theory for quantum liquids at finite temperature has been employed to evaluate the equilibrium free energy, the volumetric and gravimetric adsorption capacities, and the microscopic density profiles. The method allows one to account for the many-body and quantum delocalization effects on a single theoretical framework.

We have evaluated the binding free energies for the symmetric (n,n) carbon foams, n = 2−5, taken as the difference between the total free energy of the system and that of the homogeneous hydrogen gas at the same density and temperature. This magnitude shows the relatively fast deterioration of adsorption properties of these porous media with the increase of thermal energy. Therefore, efficient hydrogen uptake can only be achieved at low enough temperatures. At high temperatures, the approximate values of the volumetric storage capacity, derived within the independent particle model, reproduce the general trend of QLDFT results for slowly varying potentials, even at moderate external pressures. However, the ideal gas approximation produce flawed results in the presence of strong confinement, due to the breakdown of the nonideality correction, as a consequence of the sensitivity of the adsorption equilibrium constant on the specific thermodynamic conditions.

For the (2,2) armchair and zigzag carbon foams, i.e., those with smaller pore sizes, the computed volumetric and gravimetric storage capacities indicate the appearance of zero point energy effects at temperatures below T = 200−250 K. In fact, the zero-point energies, corresponding to the vibrational ground states of a single hydrogen molecule on the H_2-substrate potential energy surface inside carbon nanofoams, can be estimated to be of the order of 1 kJ mol^{-1}. Therefore, significant quantum effects can be expected for the adsorption of hydrogen on the walls of these materials at temperatures below 200 K.

It has been shown that the (5,5) zigzag structure can store a significant amount of hydrogen (n_{ads} = 36 kg/m^3, gw = 4.5%) at T = 77 K and not too high pressures (p = 100 bar). These results show that the inclusion of particle interactions leads to a qualitatively different picture of the adsorption process in these nanostructures, compared to the studies carried out within the ideal gas approximation. The strengthening of the intermolecular repulsion associated with the reduction of the nanopore volume occurs faster than the corresponding enhancement of the van der Waals attraction between the H_2 molecules and the host structure. As a consequence, only the porous environments characterized by fairly large cavities can provide efficient storage media for molecular hydrogen.

In general, the gravimetric capacities of carbon foams, at liquid nitrogen temperature, lie in the range gw ∼1−4.5%. The calculated values compare quite well with the reported experimental storage capacities of other carbonaceous materials.[9] On the other hand, at room temperature, the foam gravimetric capacities lie between 0.5 and 1.4%, while the experimental values for other carbon-based materials are below 0.7%. Therefore, we can conclude that the hydrogen uptakes of carbon foams, at T = 77 K, are similar to those of other carbon hosts, but the deterioration of their adsorption properties (with the increase of thermal energy) takes place at a slightly slower rate than for other carbon allotropes.

Finally, the close relationship between the calculated volumetric and gravimetric storage capacities and the microscopic molecular distribution was also addressed. The adsorbed fluid is found to be delocalized along the walls of the graphitic foams, thereby confirming the quasi-one-dimensional adsorption picture.

■ AUTHOR INFORMATION

Notes

■ ACKNOWLEDGMENTS

A.M.-M. acknowledges the financial support from the IMPRS of the Max Planck Institut für Physik komplexer Systeme. The work was also supported by the DFG within the priority program "SPP 1362: Porous Metal-Organic Frameworks". We thank Dr. Serguei Patchkovskii for inspiring and enlightening discussions.

■ REFERENCES

(1) Dillon, A. C.; Jones, K. M.; Bekkedahl, T. A.; Kiang, C. H.; Bethune, D. S.; Heben, M. J. *Nature* **1997**, *386*, 377−379.

(2) Wang, Q.; Johnson, J. K. *Mol. Phys.* **1998**, *95*, 299−309.

(3) Darkrim, F.; Vermesse, J.; Malbrunot, P.; Levesque, D. *J. Chem. Phys.* **1999**, *110*, 4020−4027.

(4) Okamoto, Y.; Miyamoto, Y. *J. Phys. Chem. B* **2001**, *105*, 3470−3474.

(5) Williams, K. A.; Pradhan, B. K.; Eklund, P. C.; Kostov, M. K.; Cole, M. W. *Phys. Rev. Lett.* **2002**, *88*, 165502.

(6) Hübner, O.; Glöss, A.; Fichtner, M.; Klopper, W. *J. Phys. Chem. A* **2004**, *108*, 3019−3023.

(7) Deng, W.-Q.; Xu, X.; Goddard, W. A. *Phys. Rev. Lett.* **2004**, *92*, 166103.

(8) Rowsell, J. L. C.; Yaghi, O. M. *J. Am. Chem. Soc.* **2006**, *128*, 1304−1315.

(9) Xu, W.-C.; Takahashi, K.; Matsuo, Y.; Hattori, Y.; Kumagai, M.; Ishiyama, S.; Kaneko, K.; Iijima, S. *Int. J. Hydrogen Energy* **2007**, *32*, 2504−2512.

(10) Yürüm, Y.; Taralp, A.; Veziroglu, T. *Int. J. Hydrogen Energy* **2009**, *34*, 3784−3798.

(11) Wang, Q.; Challa, S. R.; Sholl, D. S.; Johnson, J. K. *Phys. Rev. Lett.* **1999**, *82*, 956−959.

(12) Zhao, X. B.; Villar-Rodil, S.; Fletcher, A. J.; Thomas, K. M. *J. Phys. Chem. B* **2006**, *110*, 9947−9955.

(13) Avalos, L. A.; Bustos, V.; Uñac, R.; Zaera, F.; Zgrablich, G. *J. Phys. Chem. B* **2006**, *110*, 24964−24971.

(14) Targets for Onboard Hydrogen Storage Systems for Light-Duty Vehicles , 2009; http://www1.eere.energy.gov/hydrogenandfuelcells/storage/pdfs/ targets_onboard_hydro_storage_explanation.pdf.

(15) Liu, C.; Fan, Y. Y.; Liu, M.; Cong, H. T.; Cheng, H. M.; Dresselhaus, M. S. *Science* **1999**, *286*, 1127−1129.

(16) Hou, P.-X.; Xu, S.-T.; Ying, Z.; Yang, Q.-H.; Liu, C.; Cheng, H.-M. *Carbon* **2003**, *41*, 2471−2476.

(17) Zheng, Q.; Gu, A.; Lu, X.; Lin, W. *Int. J. Hydrogen Energy* **2004**, *29*, 481−489.

(18) Eletskii, A. V. *Phys.-Usp.* **2004**, *47*, 1119−1154.

(19) van den Berg, A. W. C.; Arean, C. O. *Chem. Commun.* **2008**, 668−681.

(20) Beenakker, J. J. M.; Borman, V. D.; Krylov, S. Y. *Chem. Phys. Lett.* **1995**, *232*, 379−382.

(21) Martínez-Mesa, A.; Yurchenko, S. N.; Patchkovskii, S.; Heine, T.; Seifert, G. *J. Chem. Phys.* **2011**, *135*, 214701.

(22) Chandler, D.; Wolynes, P. G. *J. Chem. Phys.* **1981**, *74*, 4078−4095.

(23) McCoy, J. D.; Rick, S. W.; Haymet, A. D. J. *J. Chem. Phys.* **1989**, *90*, 4622−4623.

(24) McCoy, J. D.; Rick, S. W.; Haymet, A. D. J. *J. Chem. Phys.* **1990**, *92*, 3034−3039.

(25) McCoy, J. D.; Rick, S. W.; Haymet, A. D. J. *J. Chem. Phys.* **1990**, *92*, 3040−3047.

(26) Gu, C.; Gao, G.-H.; Yu, Y.-X. *J. Chem. Phys.* **2003**, *119*, 488−495.

(27) Broukhno, A.; Vorontsov-Velyaminov, P. N.; Bohr, H. *Phys. Rev. E* **2005**, *72*, 046703.

(28) Sweatman, M. B. *Phys. Rev. E* **2008**, *77*, 026712.

(29) Dalfovo, F.; Lastri, A.; Pricaupenko, L.; Stringari, S.; Treiner, J. *Phys. Rev. B* **1995**, *52*, 1193−1209.

(30) Casas, M.; Dalfovo, F.; Lastri, A.; Serra, Ll.; Stringari, S. *Z. Phys. D* **1995**, *35*, 67−75.

(31) Denton, A. R.; Nielaba, P.; Ashcroft, N. W. *J. Phys.: Condens. Matter* **1997**, *9*, 4061−4080.

(32) Ancilotto, F.; Faccin, F.; Toigo, F. *Phys. Rev. B* **2000**, *62*, 17035−17042.

(33) Biben, T.; Frenkel, D. *J. Phys.: Condens. Matter* **2002**, *14*, 9077−9088.

(34) Caupin, F.; Minoguchi, T. *J. Low Temp. Phys.* **2004**, *134*, 181−186.

(35) Ancilotto, F.; Barranco, M.; Caupin, F.; Mayol, R.; Pi, M. *Phys. Rev. B* **2005**, *72*, 214522.

(36) Caupin, F.; Ancilotto, F.; Barranco, M.; Mayol, R.; Pi, M. *J. Low Temp. Phys.* **2007**, *148*, 731−736.

(37) Patchkovskii, S.; Heine, T. *Phys. Rev. E* **2009**, *80*, 031603.

(38) Lee, J.; Sohn, K.; Hyeon, T. *Chem. Commun.* **2002**, 2674−2675.

(39) Calvo, M.; García, R.; Arenillas, A.; Suárez, I.; Moinelo, S. R. *Fuel* **2005**, *84*, 2184−2189.

(40) Kaur, S.; Ajayan, P. M.; Kane, R. S. *J. Phys. Chem. B* **2006**, *110*, 21377−21380.

(41) Yu, Q.; Straatman, A. G.; Thomson, B. E. *Appl. Therm. Eng.* **2006**, *26*, 131−143.

(42) Li, S.; Song, Y.; Song, Y.; Shi, J.; Liu, L.; Wei, X.; Guo, Q. *Carbon* **2007**, *45*, 2092−2097.

(43) Karfunkel, H. R.; Dressler, T. *J. Am. Chem. Soc.* **1992**, *114*, 2285−2288.

(44) Balaban, A. T.; Klein, D. J.; Folden, C. A. *Chem. Phys. Lett.* **1994**, *217*, 266−270.

(45) Van Vechten, J. A.; Keszler, D. A. *Phys. Rev. B* **1987**, *36*, 4570−4573.

(46) Park, N.; Ihm, J. *Phys. Rev. B* **2000**, *62*, 7614−7618.

(47) Umemoto, K.; Saito, S.; Berber, S.; Tománek, D. *Phys. Rev. B* **2001**, *64*, 193409.

(48) Kuc, A.; Seifert, G. *Phys. Rev. B* **2006**, *74*, 214104.

(49) Klett, J.; Hardy, R.; Romine, E.; Walls, C.; Burcell, T. *Carbon* **2000**, *38*, 953−973.

(50) Klett, J. W.; McMillan, A. D.; Gallego, N. C.; Walls, C. A. *J. Mater. Sci.* **2004**, *39*, 3659−3676.

(51) Lee, J.; Sohn, K.; Hyeon, T. *J. Am. Chem. Soc.* **2001**, *123*, 5146−5147.

(52) Leroy, C. M.; Carn, F.; Backov, R.; Trinquecoste, M.; Delhaes, P. *Carbon* **2007**, *45*, 23017−2320.

(53) Prabhakaran, K.; Singh, P. K.; Gokhale, N. M.; Sharma, S. C. *J. Mater. Sci.* **2007**, *42*, 3894−3900.

(54) Wang, Q.; Johnson, K. *J. Chem. Phys.* **1999**, *110*, 577−586.

(55) Tanaka, H.; Kanoh, H.; Yudasaka, M.; Iijima, S.; Kaneko, K. *J. Am. Chem. Soc.* **2005**, *127*, 7511−7516.

(56) Tanaka, H.; Fan, J.; Kanoh, H.; Yudasaka, M.; Iijima, S.; Kaneko, K. *Mol. Simul.* **2005**, *31*, 465−474.

(57) Kumar, A. V. A.; Herv, J.; Bhatia, S. K. *J. Phys. Chem. B* **2006**, *110*, 16666−16671.

(58) Kowalczyk, P.; Gauden, P. A.; Terzyk, A. P.; Bhatia, S. K. *Langmuir* **2007**, *23*, 3666−3672.

(59) Noguchi, D.; Tanaka, H.; Kondo, A.; Kajiro, H.; Noguchi, H.; Ohba, T.; Kanoh, H.; Kaneko, K. *J. Am. Chem. Soc.* **2008**, *130*, 6367−6372.

(60) Kumar, A. V. A.; Bhatia, S. K. *J. Phys. Chem. C* **2008**, *112*, 11421−11426.

(61) Kowalczyk, P.; Gauden, P. A.; Terzyk, A. P. *J. Phys. Chem. B* **2008**, *112*, 8275−8284.

(62) Wang, Y.; Bhatia, S. K. *J. Phys. Chem. C* **2009**, *113*, 14953−14962.

(63) Ding, F.; Lin, Y.; Krasnov, P.; Yakobson, B. I. *J. Chem. Phys.* **2007**, *127*, 164703.

(64) Singh, A. K.; Lu, J.; Aga, R. S.; Yakobson, B. I. *J. Phys. Chem. C* **2011**, *115*, 2476−2482.

(65) Patchkovskii, S.; Heine, T. *Phys. Chem. Chem. Phys.* **2007**, *9*, 2697−2705.

(66) Mills, R. L.; Liebenberg, D. H.; Bronson, J. C.; Schmidt, L. C. *J. Chem. Phys.* **1977**, *66*, 3076−3084.

(67) Patchkovskii, S.; Tse, J. S.; Yurchenko, S. N.; Zhechkov, L.; Heine, T.; Seifert, G. *Proc. Natl. Acad. Sci. U.S.A.* **2005**, *102*, 10439−10444.

(68) Heine, T.; Zhechkov, L.; Seifert, G. *Phys. Chem. Chem. Phys.* **2004**, *6*, 980−984.

(69) Kuc, A.; Zhechkov, L.; Patchkovskii, S.; Seifert, G.; Heine, T. *Nano Lett.* **2007**, *1*, 1−5.

(70) Diep, P.; Johnson, J. K. *J. Chem. Phys.* **2000**, *113*, 3480−3481.